Activating Lattice Oxygen in High-Entropy LDH for Robust and Durable Water Oxidation

Fangqing Wang[a, b], Peichao Zou[c], Yangyang Zhang[b], Wenli Pan[d], Ying Li[a, b], Limin Liang[b], Cong Chen[b], Hui Liu[a, b*] and Shijian Zheng [a, b*]

[a] Key Laboratory of Special Functional Materials for Ecological Environment and Information (Ministry of Education), Hebei University of Technology, Tianjin 300130, P. R. China

[b] School of Material Science and Engineering, Hebei University of Technology, Tianjin 300130, P. R. China

[c] Department of Physics and Astronomy, University of California, Irvine, CA 92697, USA

[d] Graduate School of Human and Environmental Studies, Kyoto University, Yoshida-nihonmatsu-cho, Sakyo, Kyoto 606-8501, Japan

E-mail: liuhui2013@hebut.edu.cn (Hui Liu); sjzheng@hebut.edu.cn (Shijian Zheng)

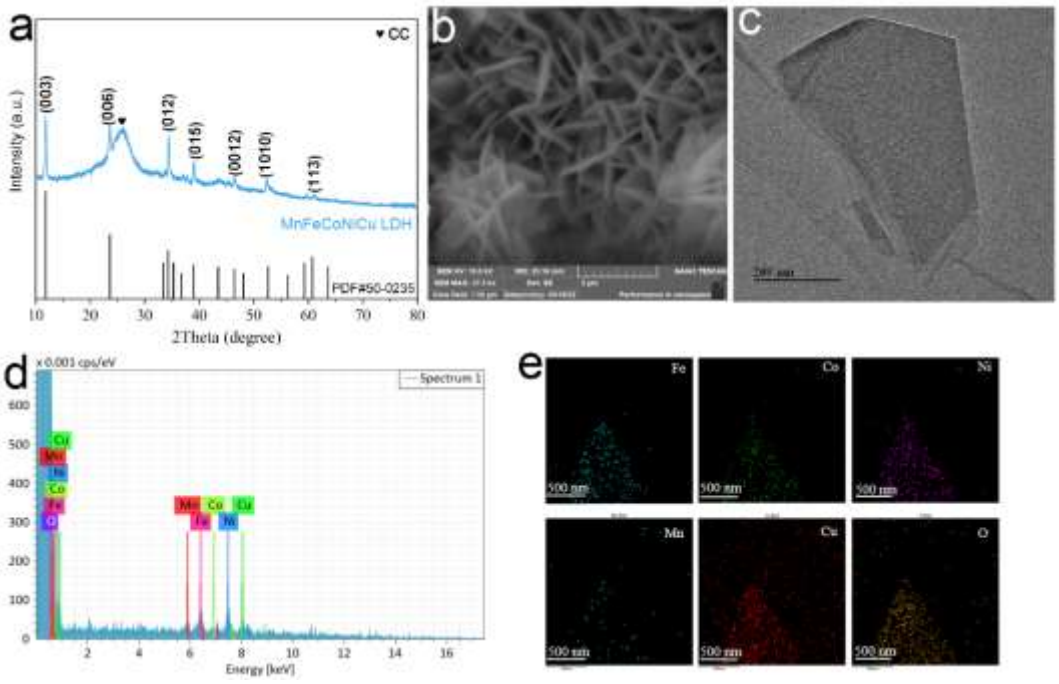

Figure S1. (a) XRD pattens, (b) SEM image, (c) TEM image, (d) EDS spectrum and

(e) mapping of MnFeCoNiCu LDH.

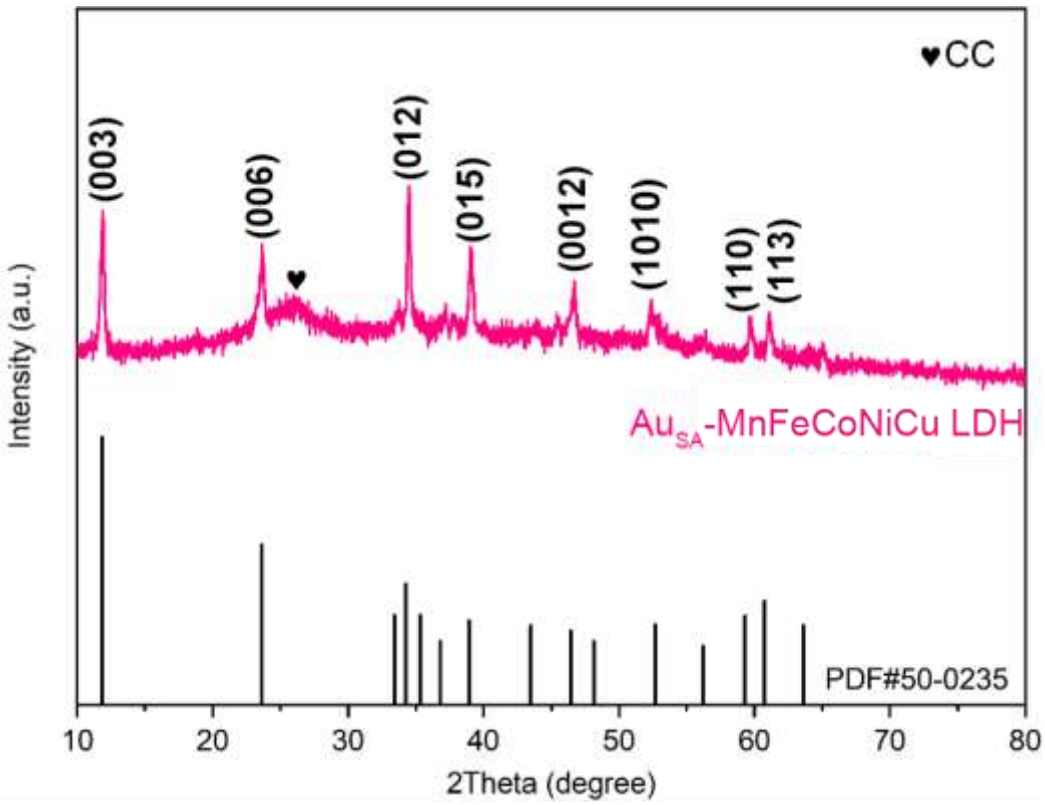

Figure S2. XRD pattens of Au_{SA}-MnFeCoNiCu LDH.

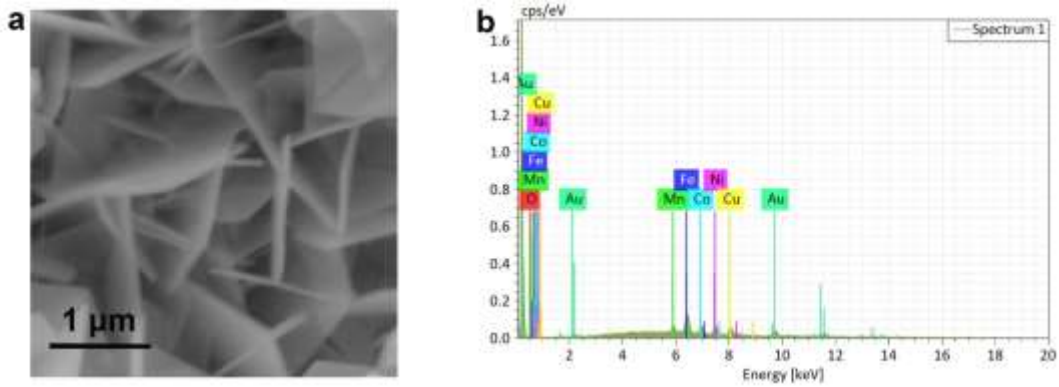

Figure S3. (a) SEM image and (b) EDS spectrum of Au_{SA}-MnFeCoNiCu LDH.

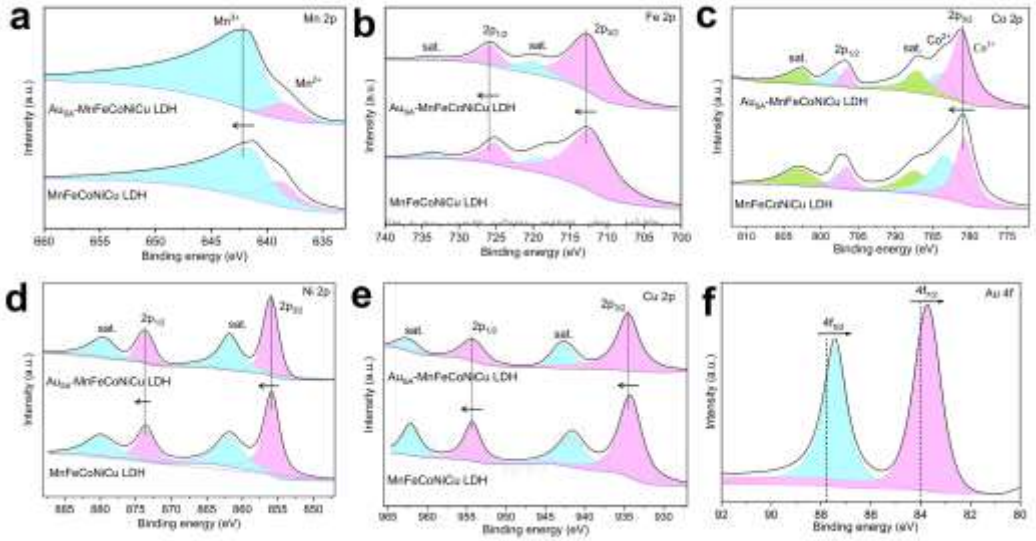

Figure S4. High-resolution XPS spectra of (a) Mn 2p, (b) Fe 2p, (c) Co 2p, (d) Ni 2p, (e) Cu 2p of Au_{SA}-MnFeCoNiCu LDH and MnFeCoNiCu LDH. (f) Au 4f of Au_{SA}-MnFeCoNiCu LDH.

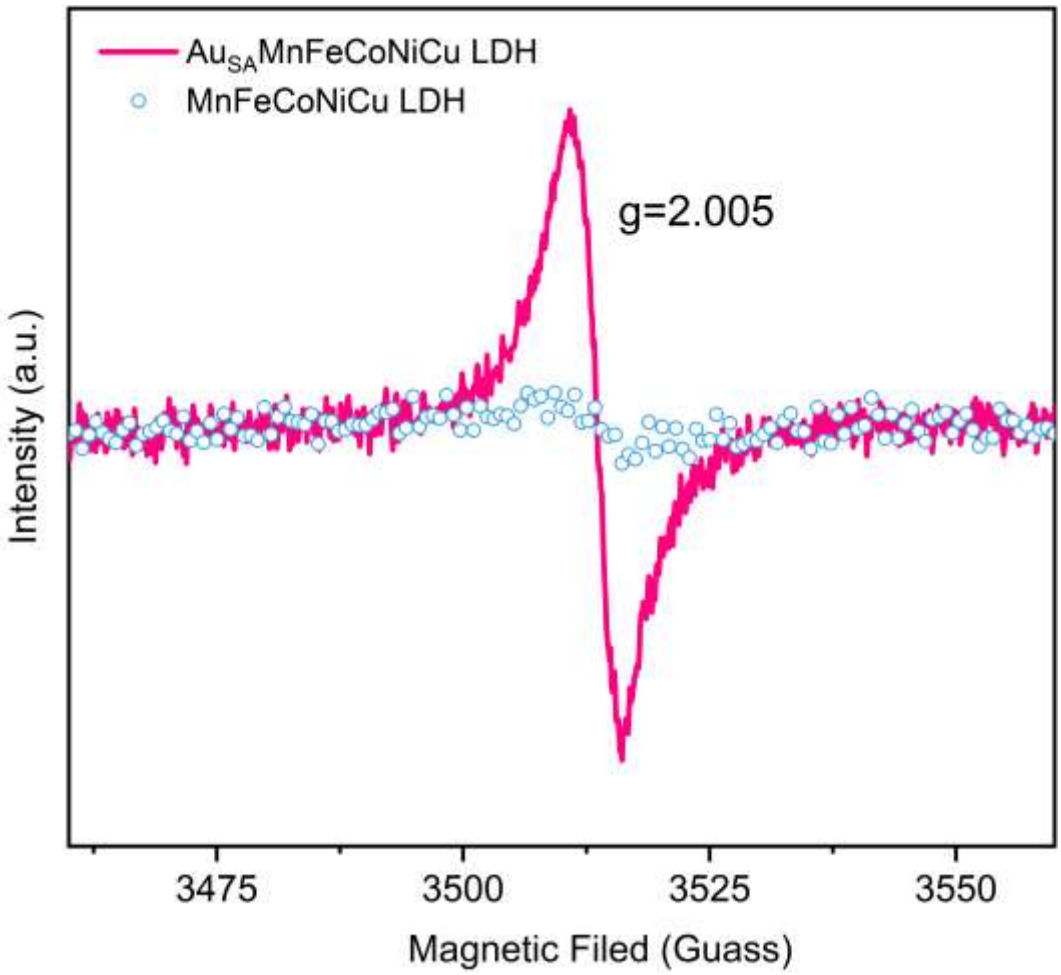

Figure S5. EPR spectra of Au_{SA}-MnFeCoNiCu LDH and MnFeCoNiCu LDH.

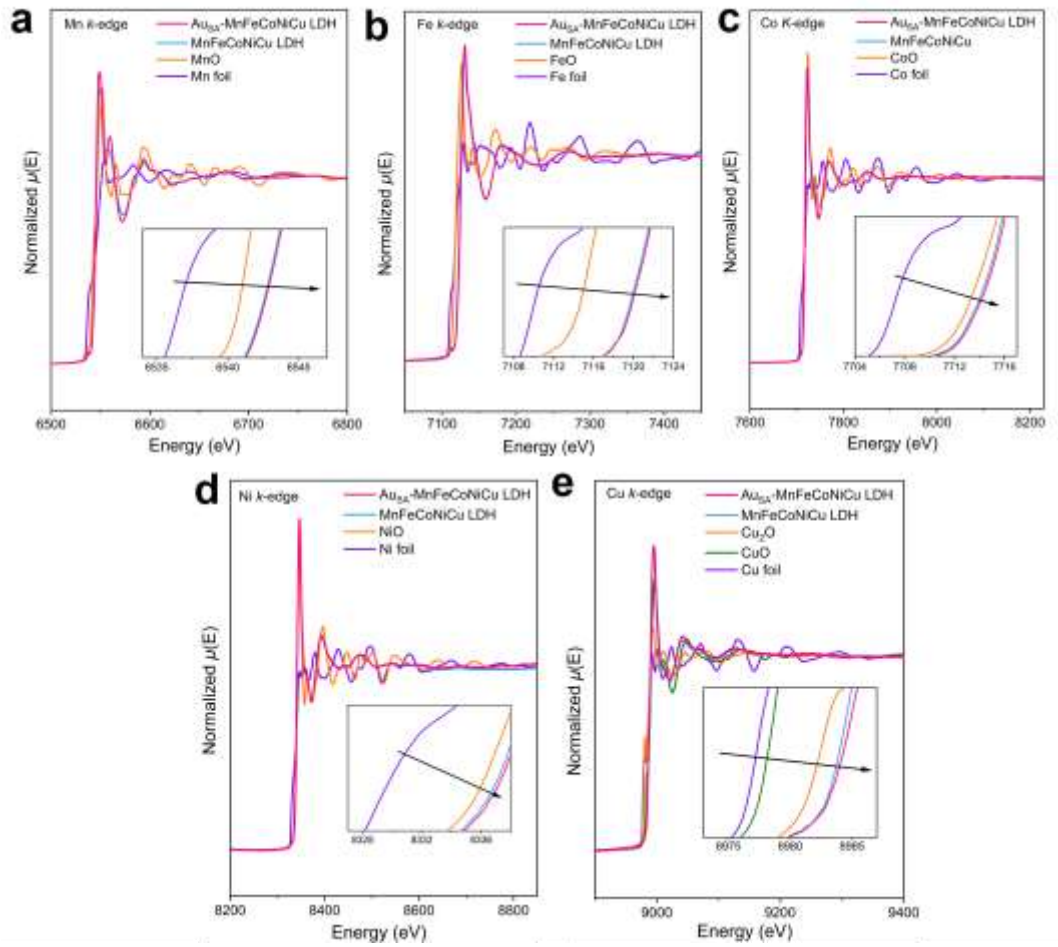

Figure S6. Normalized *K*-edge XAFS spectra of Mn, Fe, Co, Ni and Cu elements.

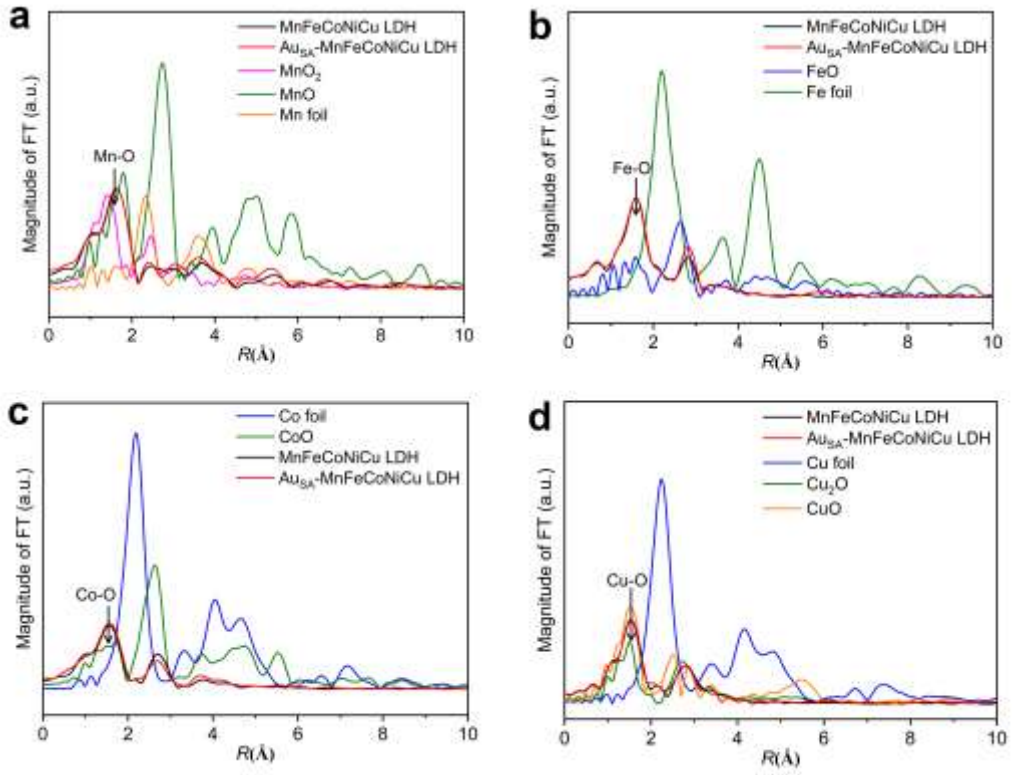

Figure S7. FT-EXAFS spectra and fitting results of Mn, Fe, Co and Cu elements.

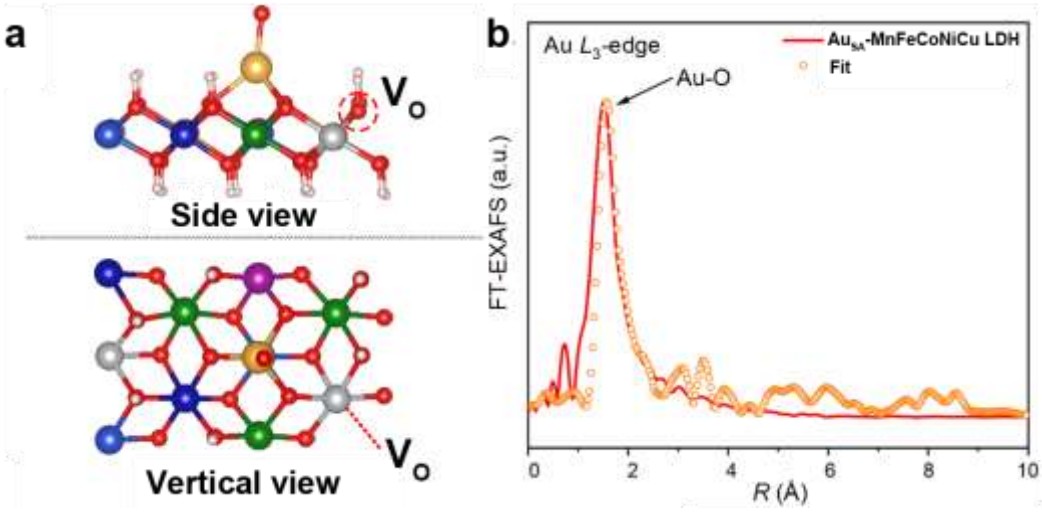

Figure S8. (a) The model in which Au is directly anchored by surface oxygen. (b) The corresponding EXAFS k^2 $\chi(k)$ Fourier transform (FT) spectra of Au$_{SA}$-MnFeCoNiCu LDH and fitting curve (Gray: Ni, Green: Fe, Navy: Co, Purple: Mn, Light Blue: Cu; Yellow: Au; Red: O; White: H).

Figure S9. Model of Au Atom Replacing Surface (a) Fe, (b) Co, (c) Ni, (d) Mn, (e) Cu Sites (Gray: Ni, Green: Fe, Navy: Co, Purple: Mn, Light Blue: Cu; Yellow: Au; Red: O; White: H).

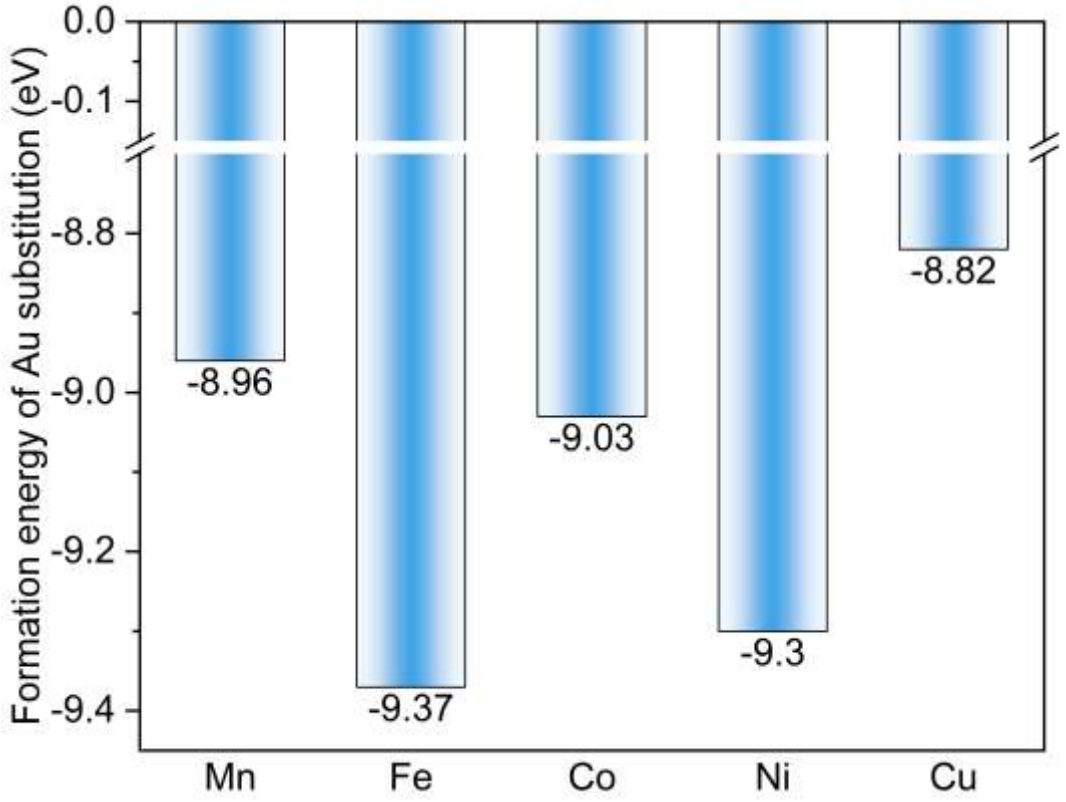

Figure S10. Calculated the substitution formation energies of Au_M (M=Fe, Co, Ni, Mn and Cu) via DFT. Au is easier to replace Fe (-9.37 eV) than Mn (-8.96 eV), Co (-9.03 eV), Ni (-9.30 eV) and Cu (-8.82 eV).

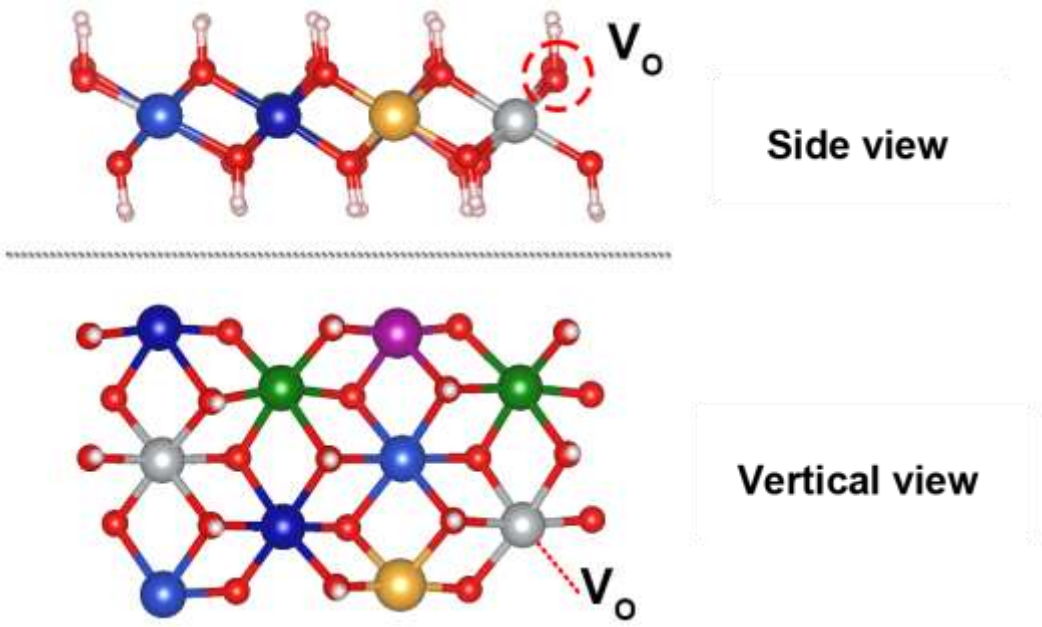

Figure S11. Model of Au occupying Fe site (Gray: Ni, Green: Fe, Navy: Co, Purple: Mn, Light Blue: Cu; Yellow: Au; Red: O; White: H).

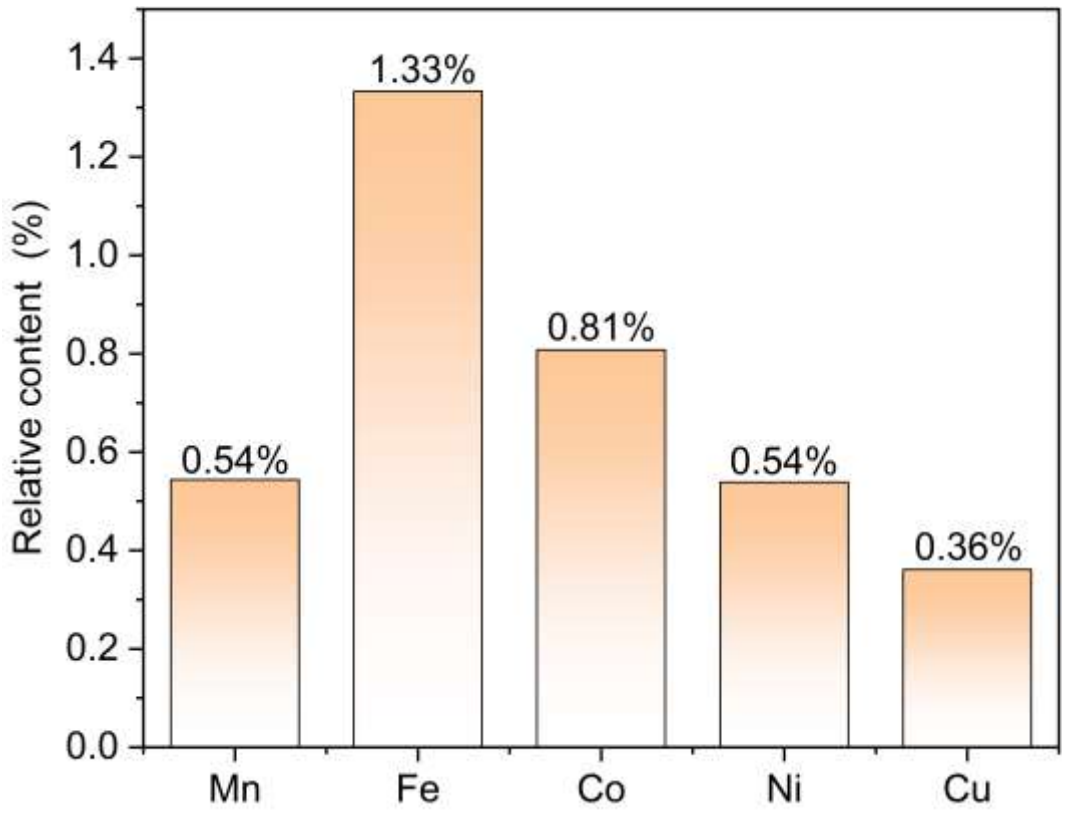

Figure S12. The proportion of metal elements dissolved in the electrolyte to the metal

elements in the original sample during the CV process of MnFeCoNiCu LDH measured by ICP-MS, which stands for the metal dissolution percentage. Calculation method: the relative content is the ratio of the mass of a metal element (Mn, Fe, Co, Ni and Cu) dissolved in the electrolyte after CV to the mass of the element in the original sample, shown as formula below.

$$\text{Relative content} = \frac{C_d \times V}{C_o \times m} \times 100\%$$

Here C_d (mg L^{-1}) is the dissolved concentration of the element in the electrolyte after CV test, V (L) is the volume of electrolyte during CV test, C_0 (mg kg^{-1}) is the original loading content of the element on the electrode before CV test, and m (kg) is the mass of electrode.

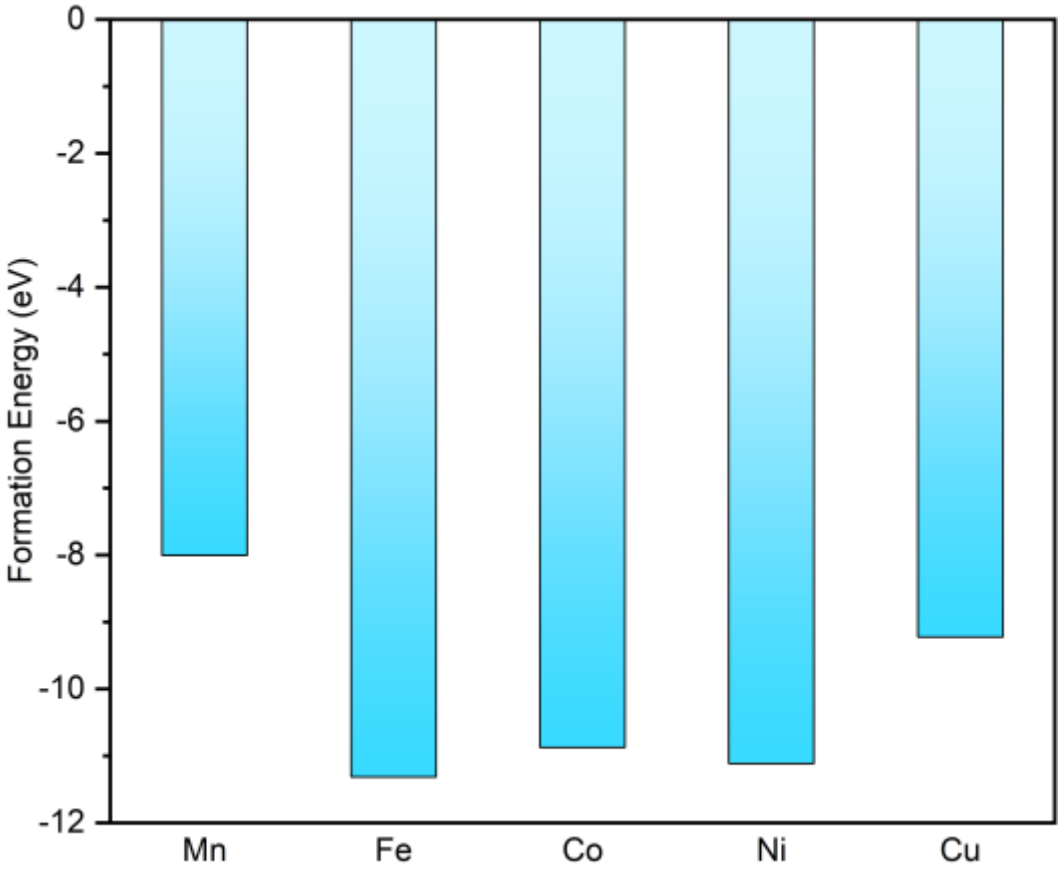

Figure S13. Metal-vacancy formation energy of Au_{SA}-MnFeCoNiCu LDH. From the

thermodynamic point of view, from a thermodynamic perspective, Fe vacancies are more likely to form.

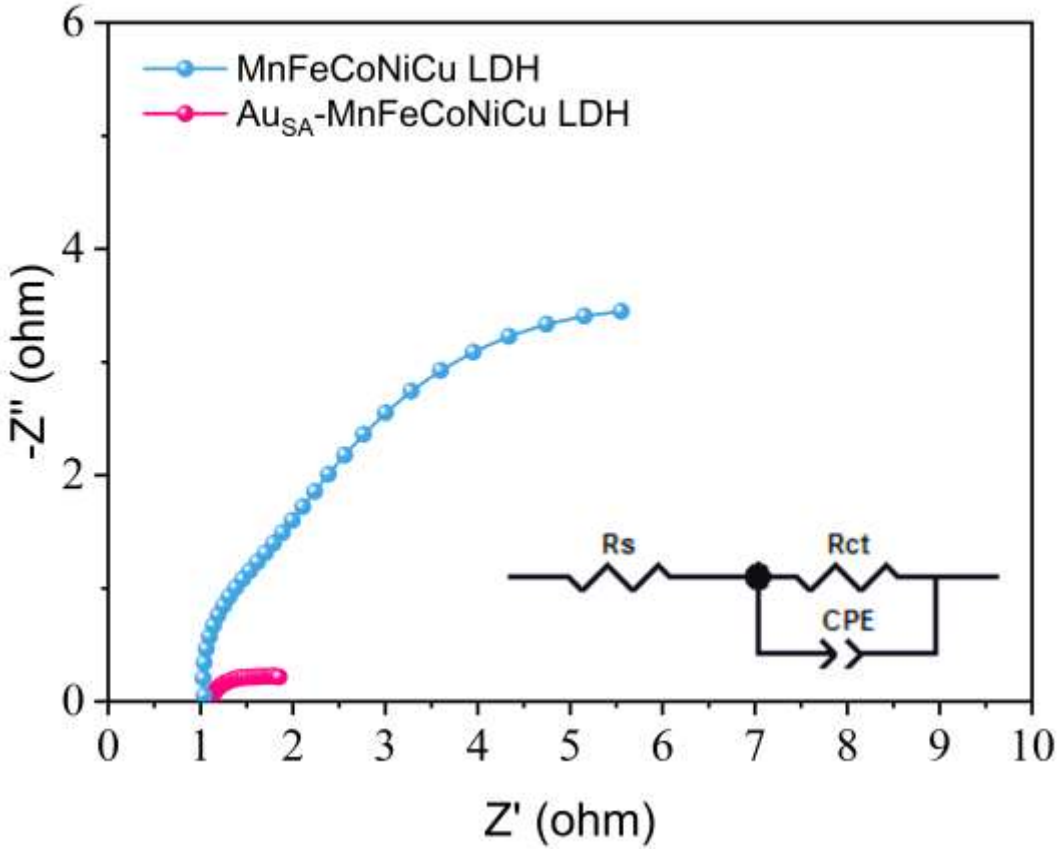

Figure S14. EIS curves of Au$_{SA}$-MnFeCoNiCu LDH and MnFeCoNiCu LDH (inset is equivalent circuit).

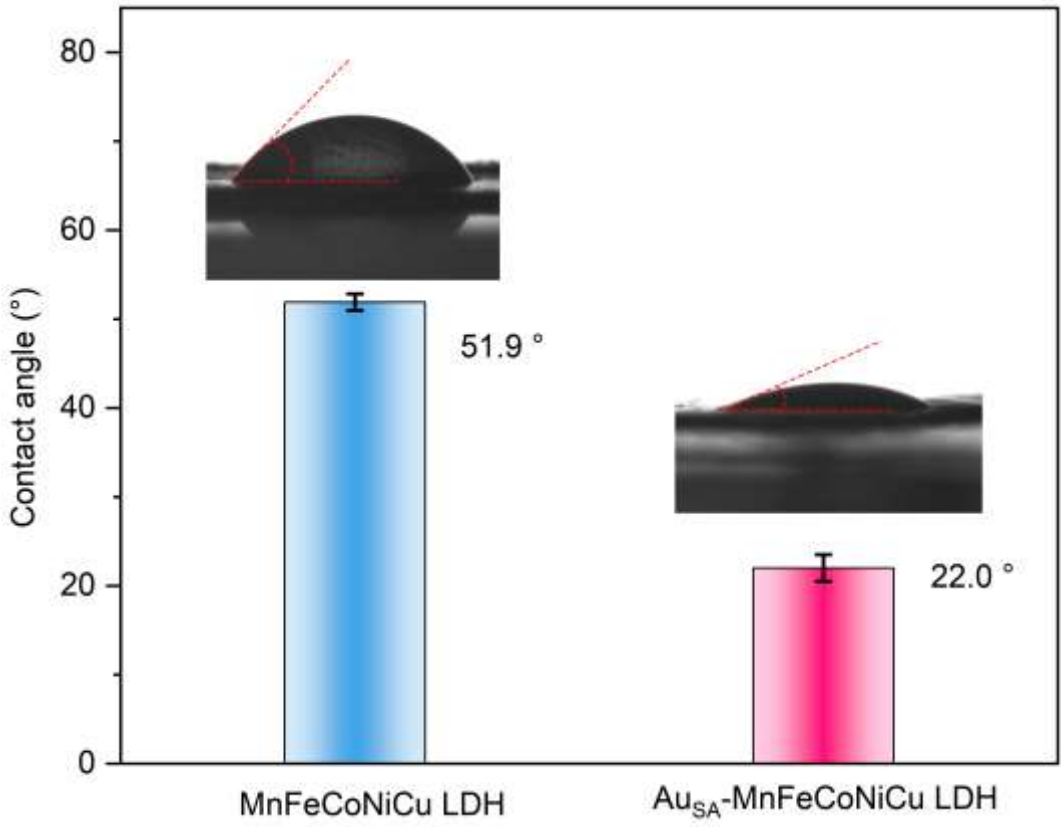

Figure S15. Contact angle of liquid drop on catalyst surface.

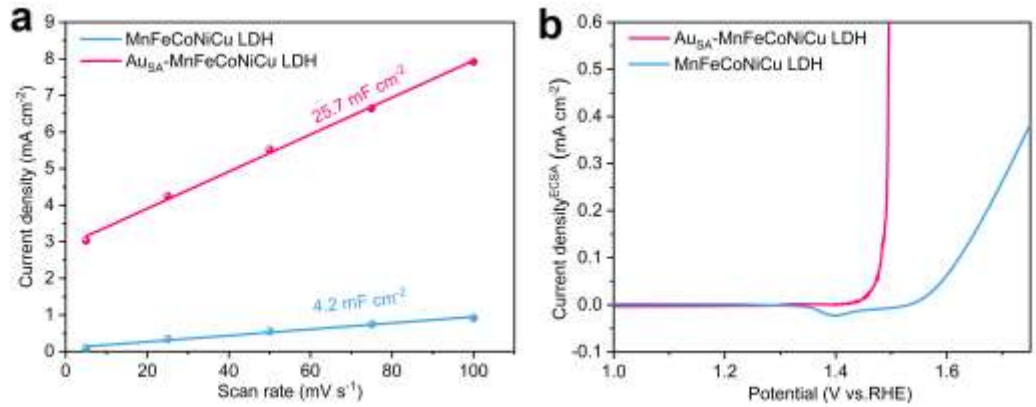

Figure S16. (a) C_{dl} curves, (b) LSV curves normalized by ECSA of the Au$_{SA}$-MnFeCoNiCu LDH and MnFeCoNiCu LDH.

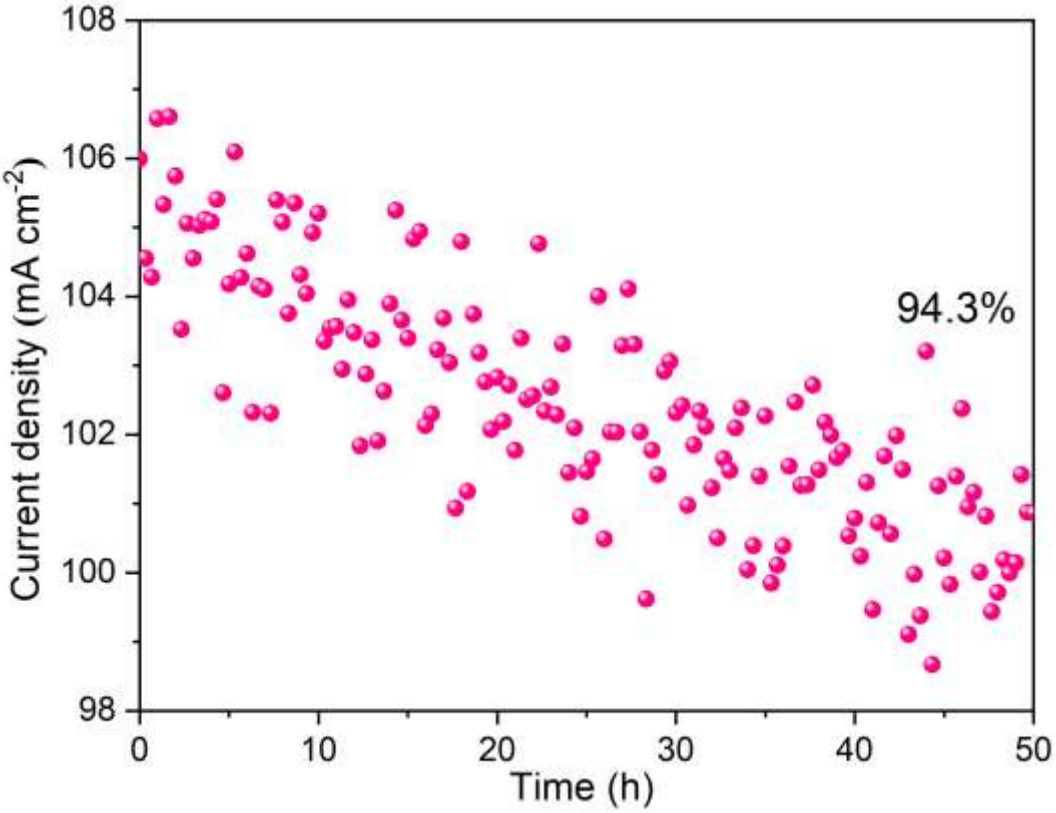

Figure S17. Stability test of Au_{SA}-MnFeCoNiCu LDH at the initial 50 h, activity decay is 94.3 %.

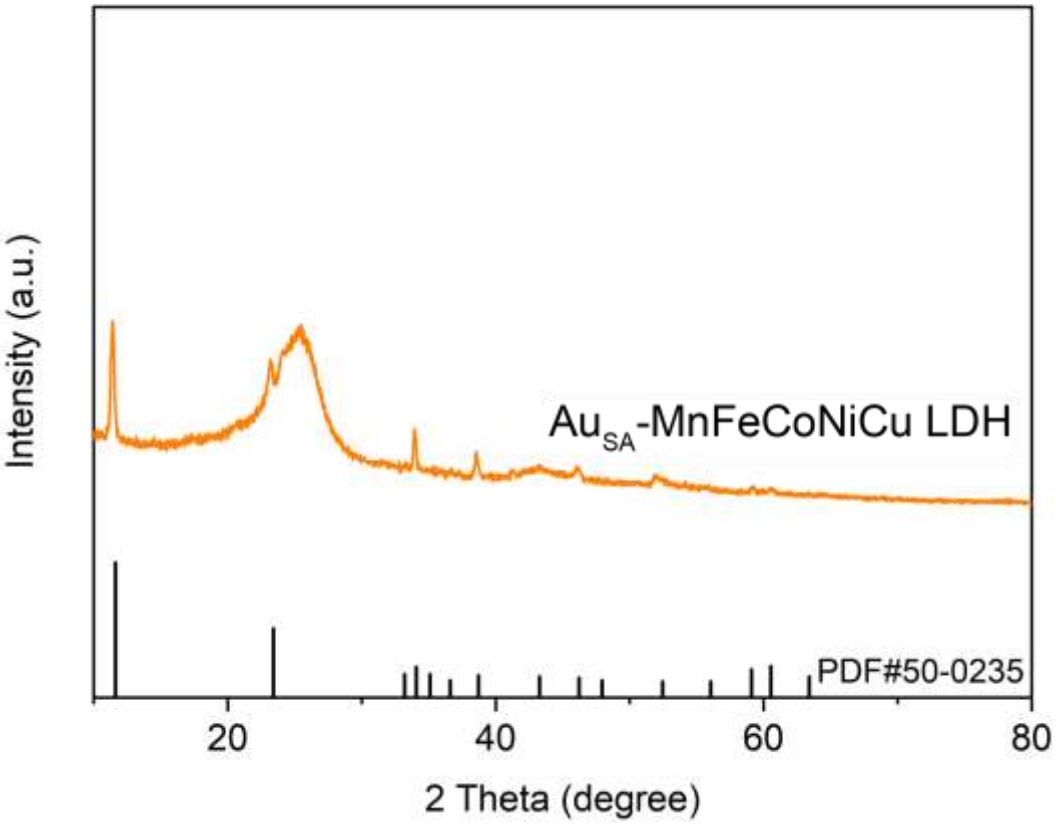

Figure S18. XRD pattens of Au_{SA}-MnFeCoNiCu LDH after 50 h Stability test.

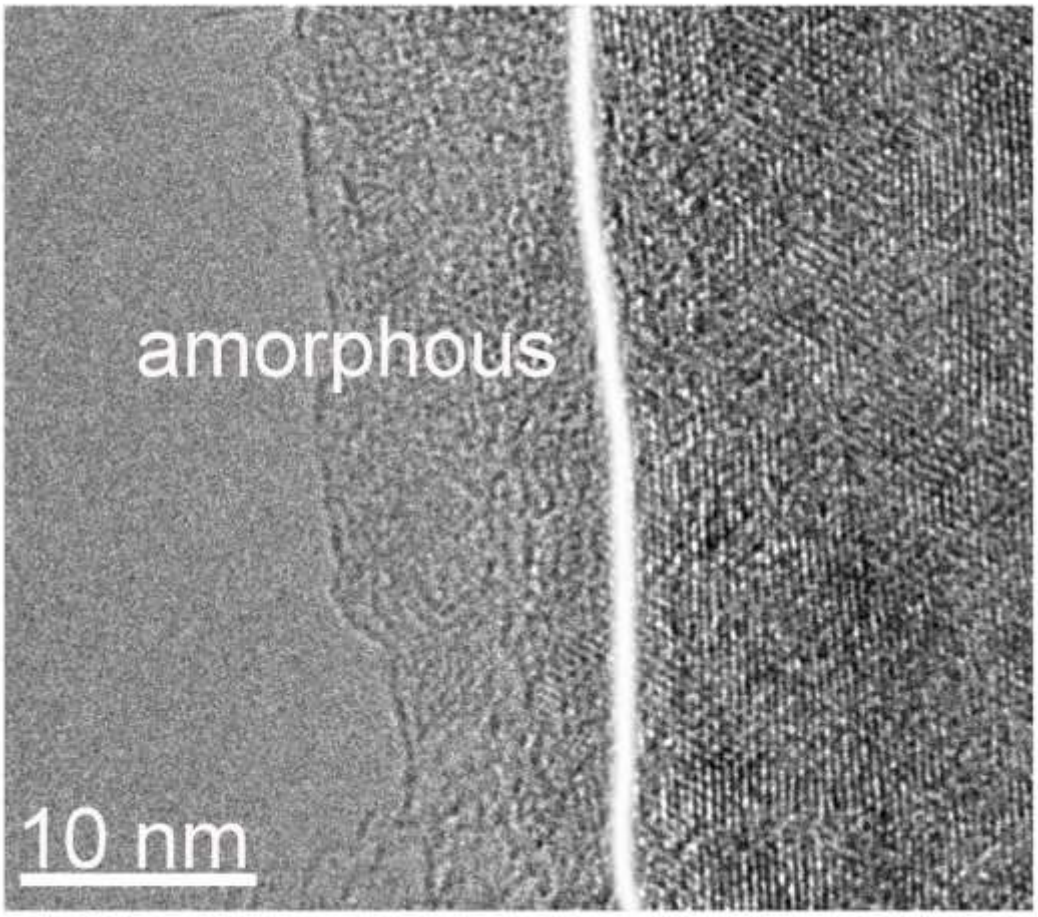

Figure S19. HR-TEM images of Au_{SA}-MnFeCoNiCu LDH after 50 h long-term OER test.

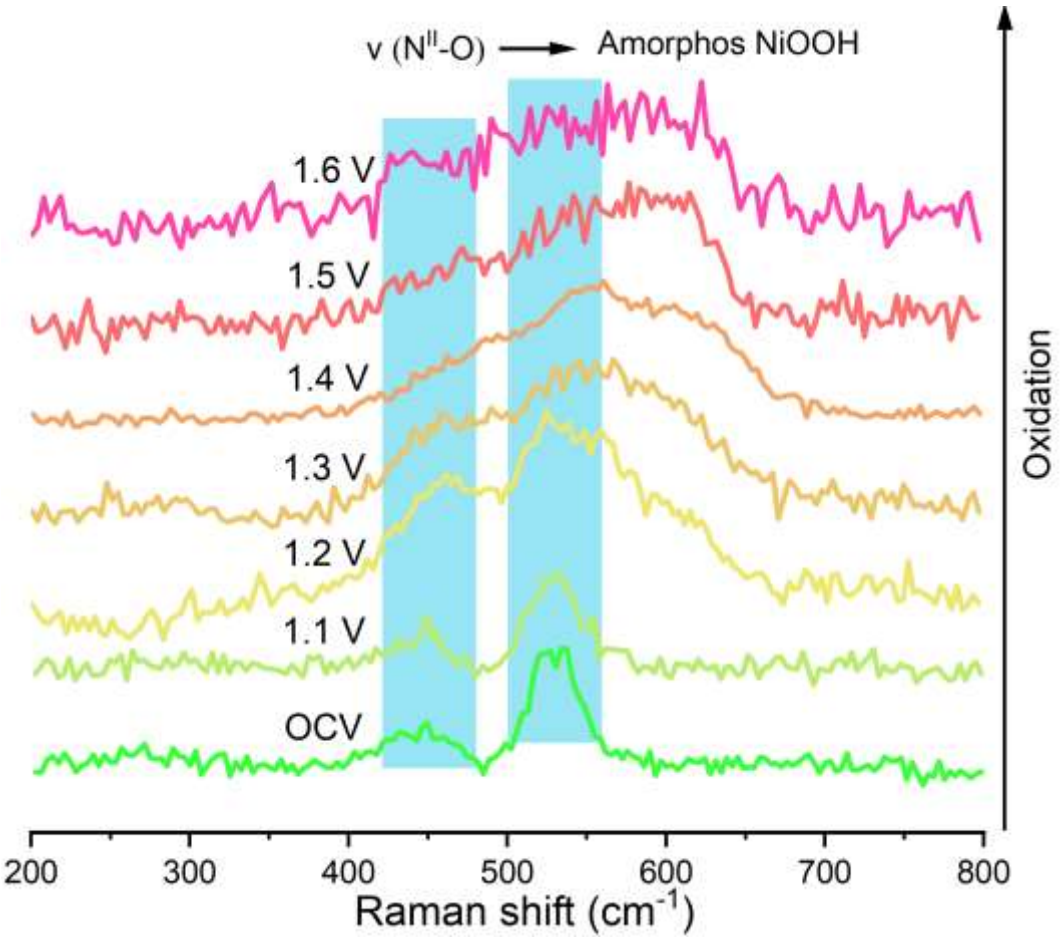

Figure S20. In situ Raman spectra of Au_{SA}-MnFeCoNiCu LDH. With the increase of the OER potential, two narrow peaks corresponding to the Ni^{II}-O bond gradually weaken until they disappear, while a broad peak gradually appears, which corresponds to the NiOOH species. It indicates that with the OER process, the $Ni(OH)_x$ on the Au_{SA}-MnFeCoNiCu LDH surface gradually transforms to the non-characterized NiOOH.

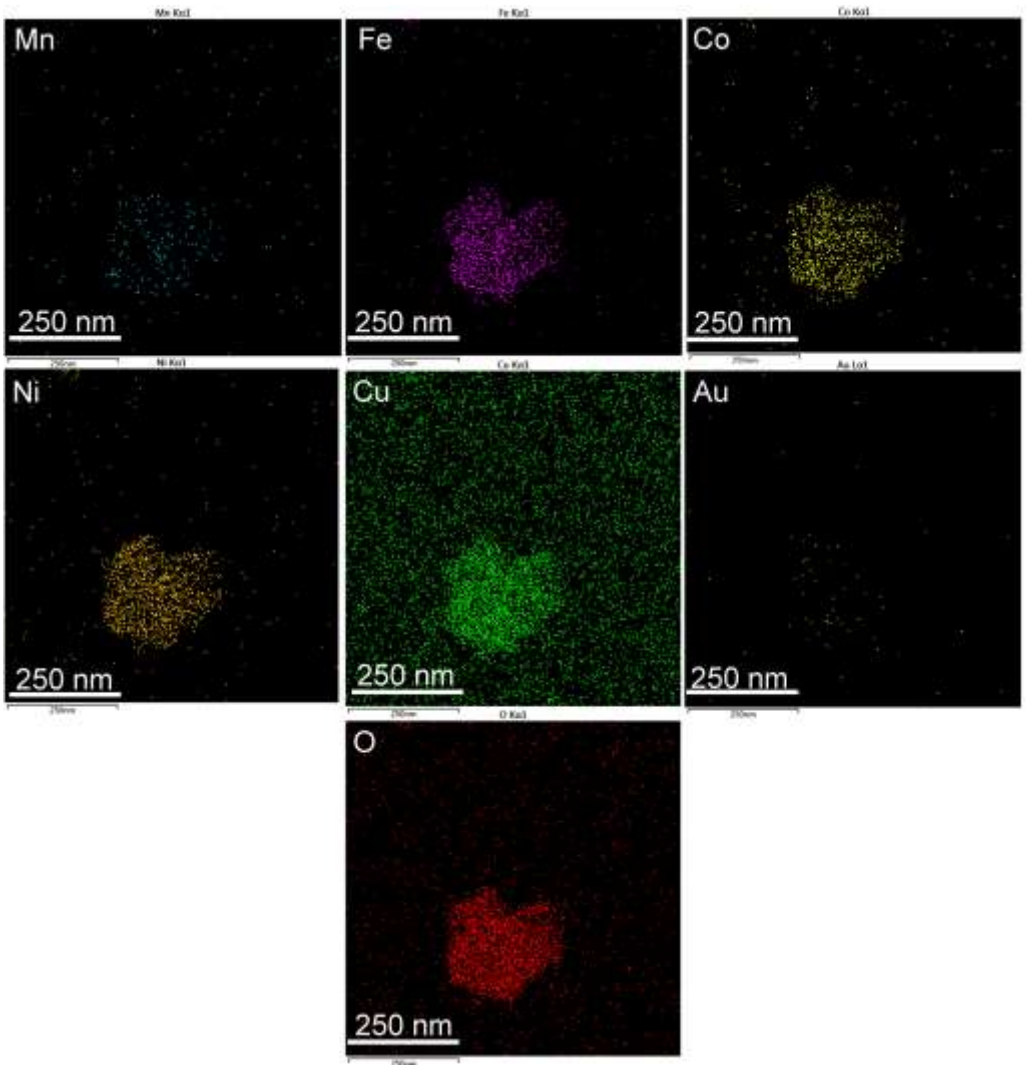

Figure S21. Element mapping of Au_{SA}-MnFeCoNiCu LDH after 50 h long-term OER test.

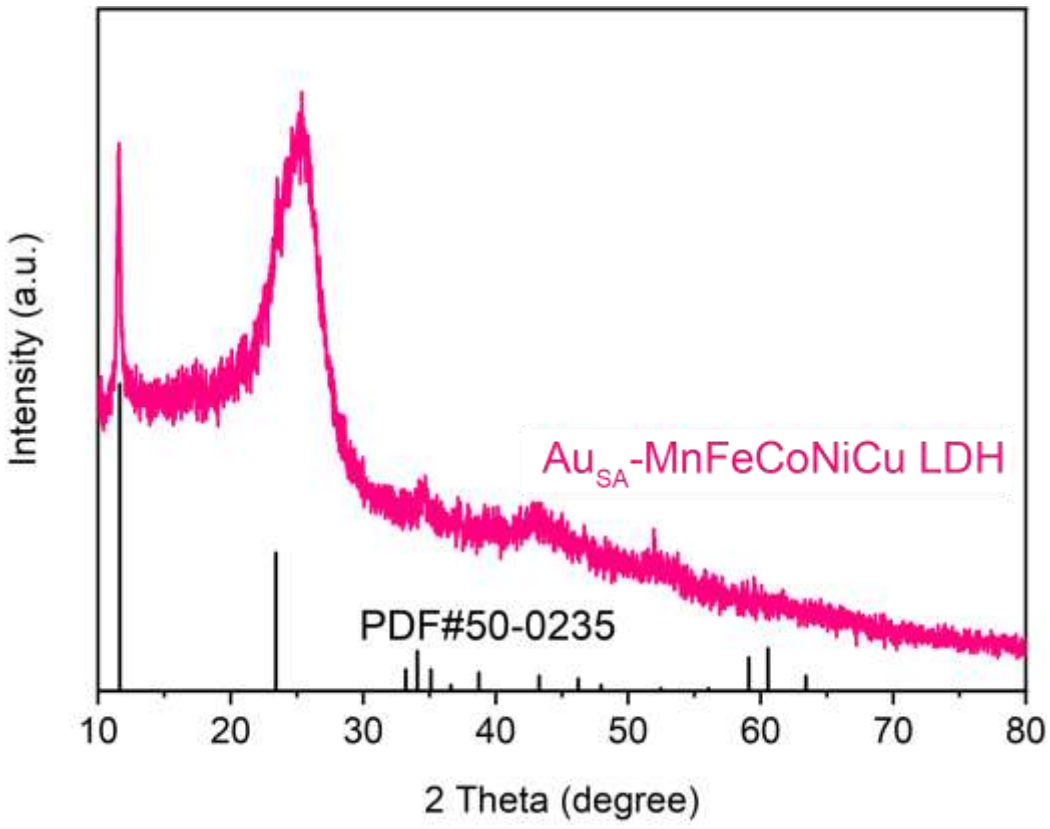

Figure S22. XRD pattens of Au_{SA}-MnFeCoNiCu LDH after long-term OER test.

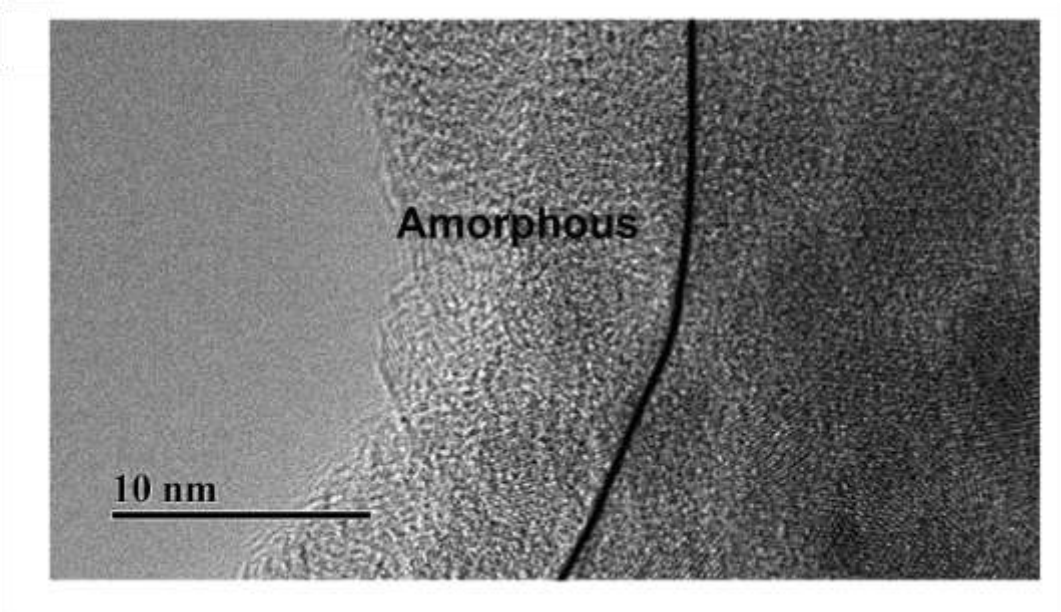

Figure S23. HRTEM image of Au_{SA}-MnFeCoNiCu LDH after long-term OER test.

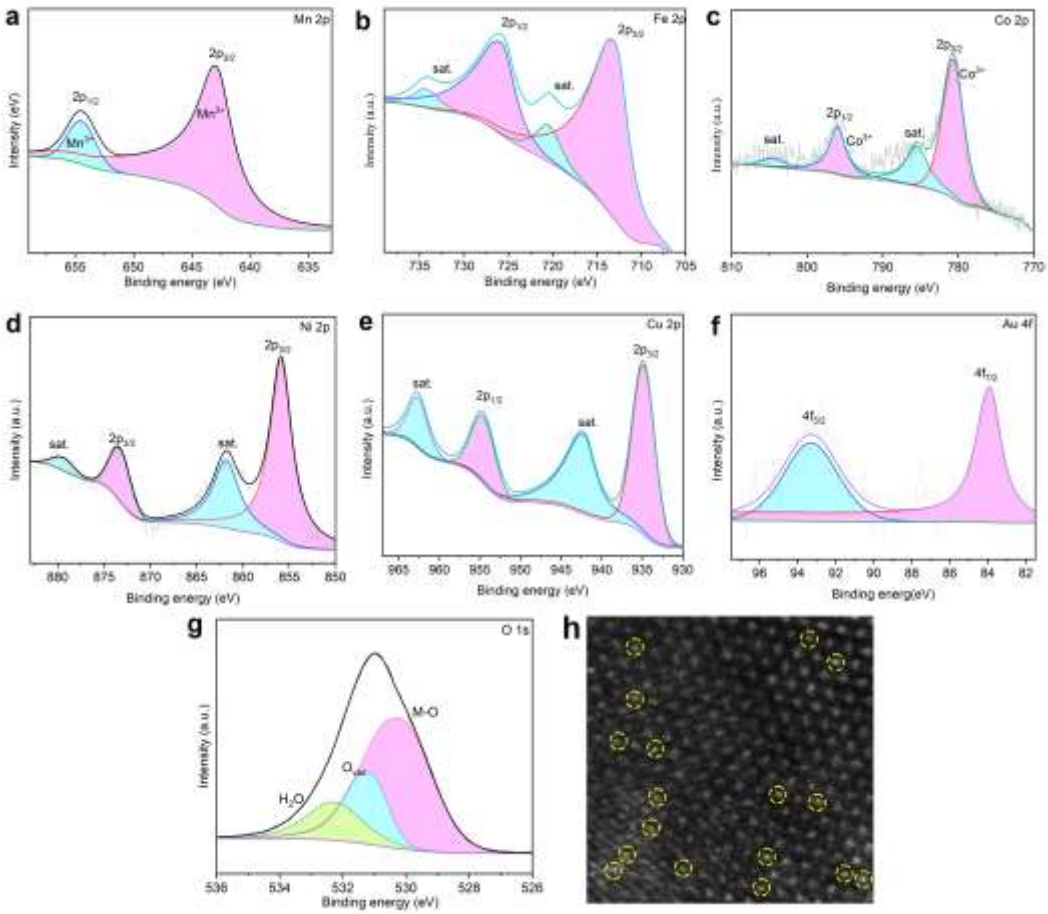

Figure S24. High-resolution XPS spectra of (a) Mn 2p, (b) Fe 2p, (c) Co 2p, (d) Ni 2p, (e) Cu 2p (f) Au 4f and (g) O 1s of Au_{SA}-MnFeCoNiCu LDH after stability test. (h) AC-HAADF-STEM image of Au_{SA}-MnFeCoNiCu LDH after stability test.

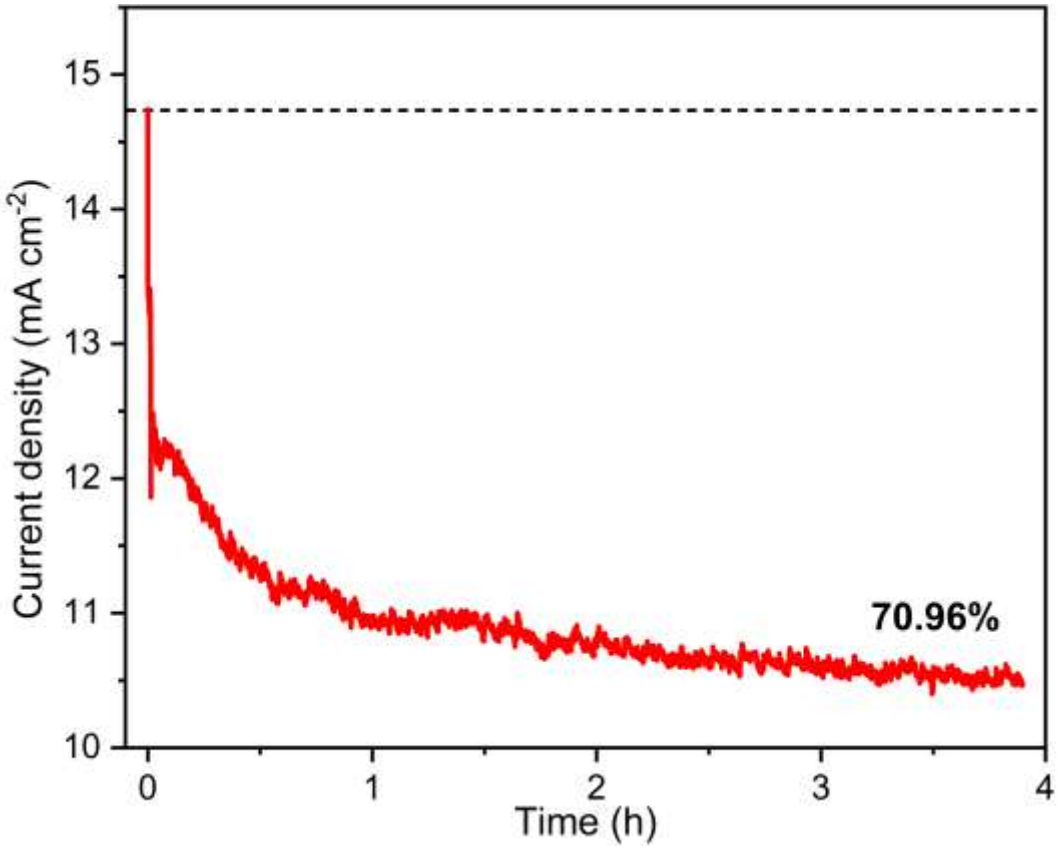

Figure S25. Stability test of NiFe LDH.

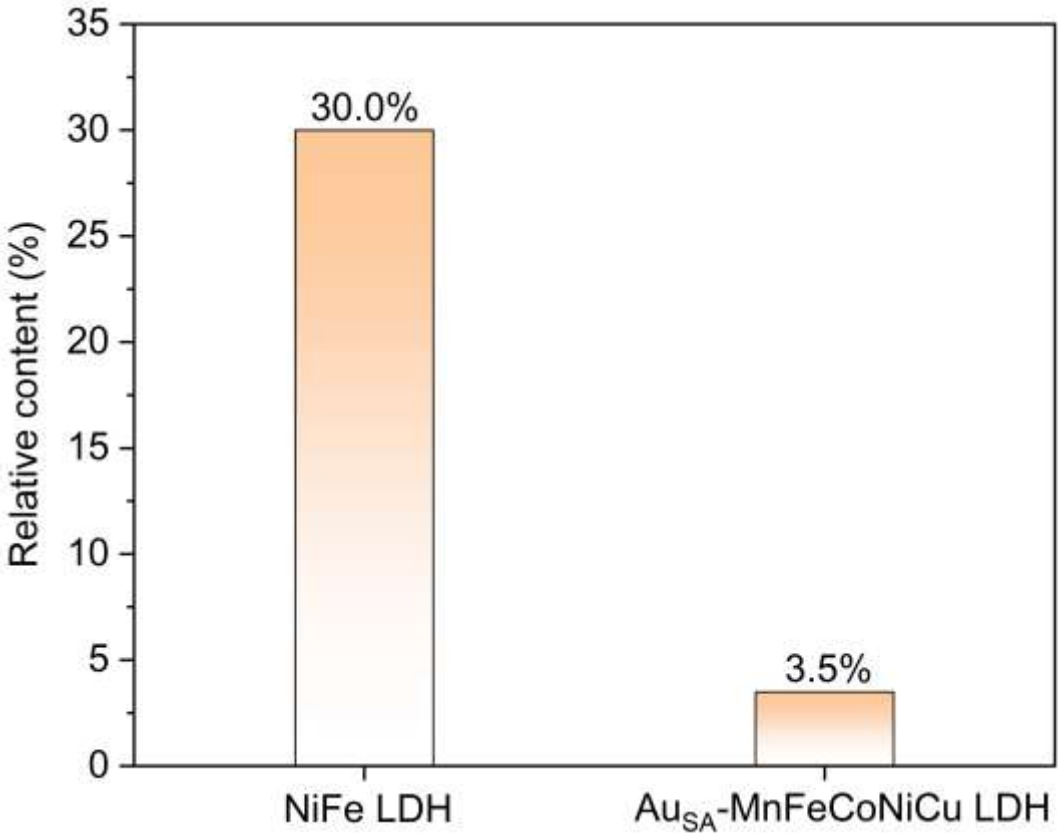

Figure S26. After the stability test of NiFe LDH and Au_{SA}-MnFeCoNiCu LDH, the proportion of Fe element dissolved in the electrolyte to the Fe element in the original sample, which stands for the Fe dissolution percentage. The calculation method is similar to Figure S12.

$$\text{Relative content} = \frac{C_d \times V}{C_o \times m} \times 100\%$$

Here C_d (mg L^{-1}) is the dissolved concentration of the Fe element in the electrolyte after stability test, V (L) is the volume of electrolyte during stability test, C_0 (mg kg^{-1}) is the original loading content of the Fe element on the electrode before stability test, and m (kg) is the mass of electrode.

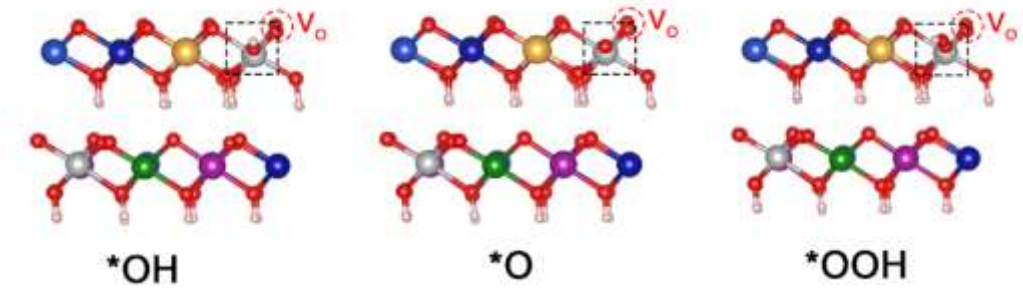

Figure S27. The theoretical models of AEM on Au_{SA}-MnFeCoNiCuOOH involved the adsorption of *OH, *O, *OOH (Ni is active site). (Gray: Ni, Green: Fe, Navy: Co, Purple: Mn, Light Blue: Cu; Yellow: Au; Red: O; White: H).

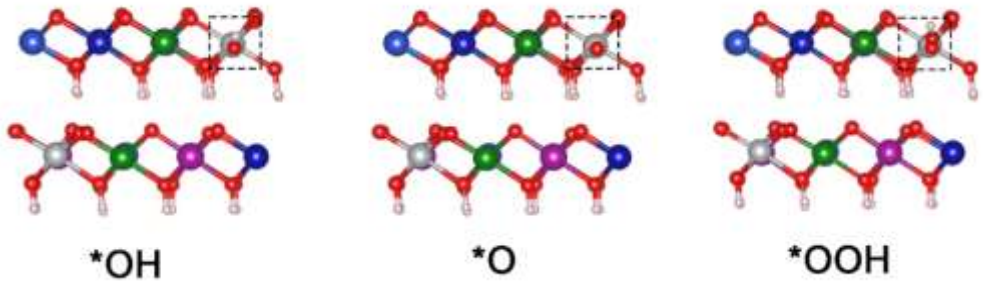

Figure S28. The theoretical models of AEM on MnFeCoNiCuOOH involved the adsorption of *OH, *O, *OOH (Ni is active site). (Gray: Ni, Green: Fe, Navy: Co, Purple: Mn, Light Blue: Cu; Red: O; White: H).

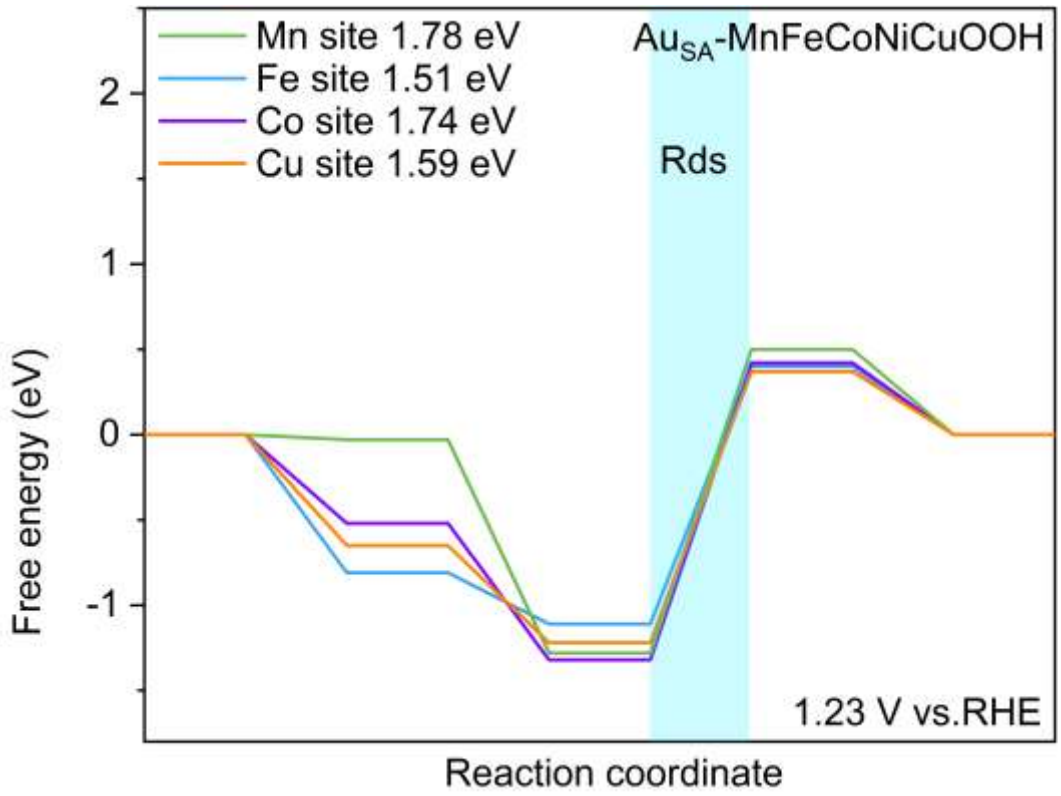

Figure S29. Free energy profiles (AEM) for Mn Fe, Co, Ni and Cu sites of Au_{SA}-MnFeCoNiCuOOH.

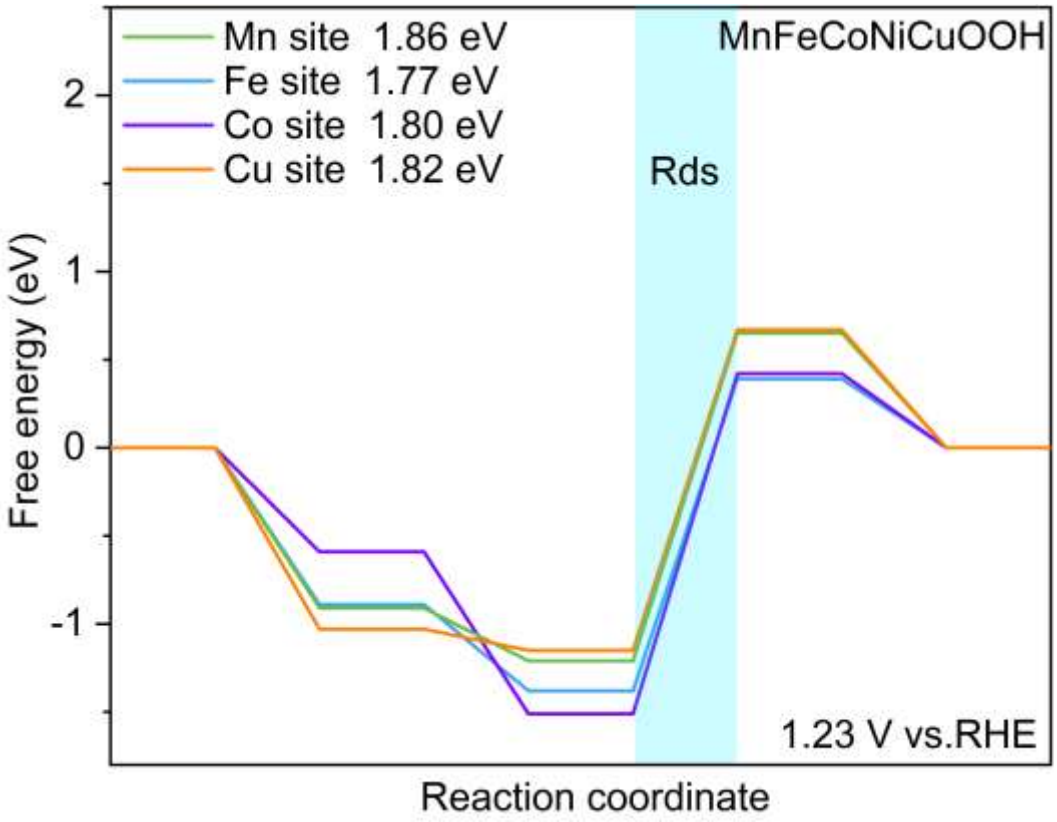

Figure S30. Free energy profiles (AEM) for Mn Fe, Co, Ni and Cu sites of MnFeCoNiCuOOH.

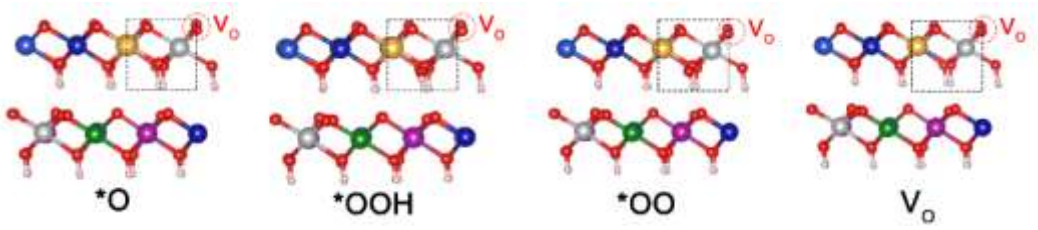

Figure S31. The theoretical models of LOM on Au_{SA}-MnFeCoNiCuOOH involved the adsorption of *O, *OOH, *OO, Vo. (Gray: Ni, Green: Fe, Navy: Co, Purple: Mn, Light Blue: Cu; Yellow: Au; Red: O; White: H).

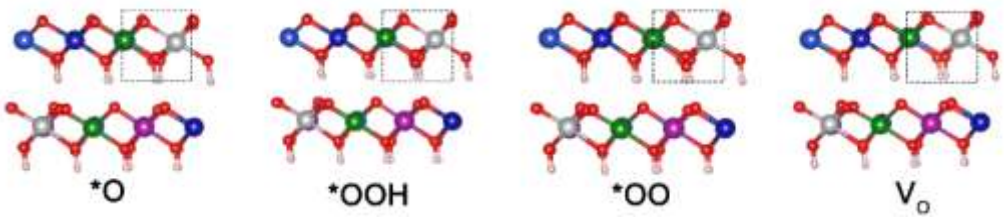

Figure S32. The theoretical models of LOM on MnFeCoNiCuOOH involved the adsorption of *O, *OOH, *OO, Vo. (Gray: Ni, Green: Fe, Navy: Co, Purple: Mn, Light Blue: Cu; Red: O; White: H).

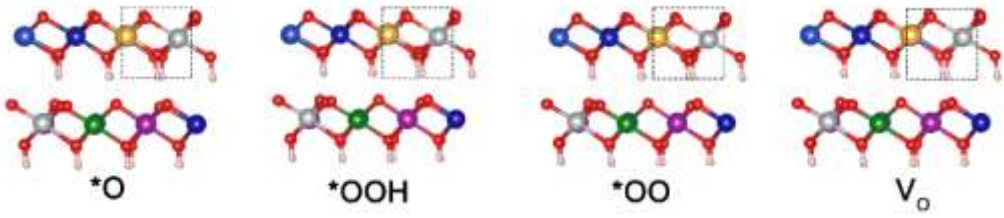

Figure S33. The theoretical models of LOM on MnFeCoNiCuOOH with only Au atoms involved the adsorption of *O, *OOH, *OO, Vo. (Gray: Ni, Green: Fe, Navy: Co, Purple: Mn, Light Blue: Cu; Yellow: Au; Red: O; White: H).

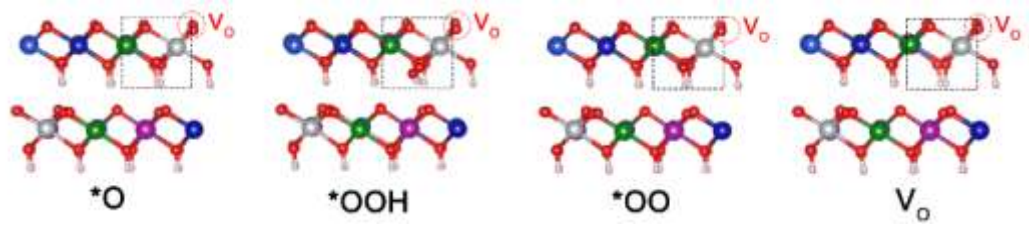

Figure S34. The theoretical models of LOM on MnFeCoNiCuOOH with only O vacancies involved the adsorption of *O, *OOH, *OO, Vo. (Gray: Ni, Green: Fe, Navy: Co, Purple: Mn, Light Blue: Cu; Red: O; White: H).

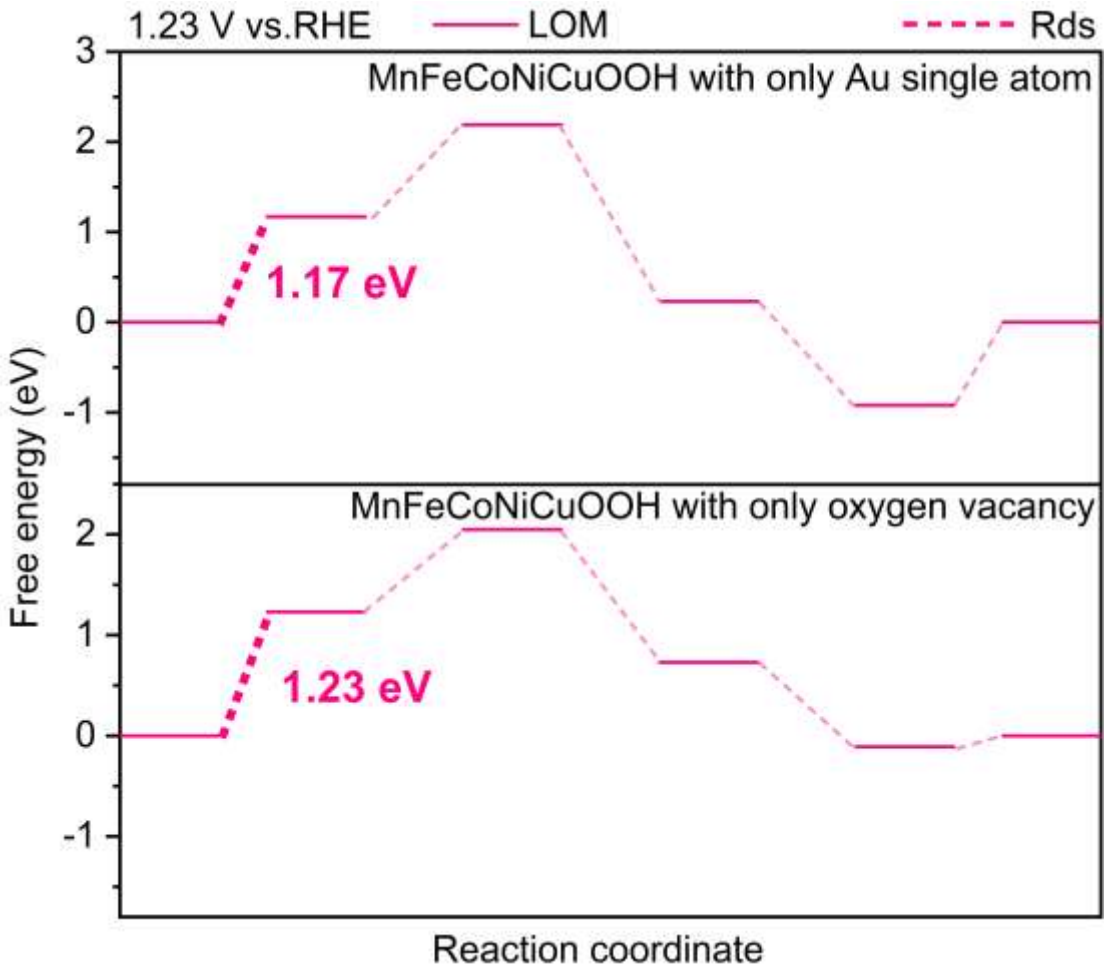

Figure S35. Free energies of OER via LOM on MnFeCoNiCuOOH with only Au atom and MnFeCoNiCuOOH with only O vacancy.

Table S1. EDS results of MnFeCoNiCu LDH and Au_{SA}-MnFeCoNiCu LDH.

	Mn (at%)	Fe (at%)	Co (at%)	Ni (at%)	Cu (at%)	Au (at%)	O (at%)
MnFeCoNiCu LDH	3.31	7.88	4.16	8.54	7.38	-	68.73
Au_{SA}-MnFeCoNiCu LDH	4.23	9.65	5.65	9.56	7.62	0.26	63.03

Table S2. Fitting result of FT-EXAFS curves shown in **Figure 2c and 2d**.

	Bond type	N	R(Å)	σ^2 ($\times10^{-3}$Å)
Au_{SA}-MnFeCoNiCu LDH	Au-O	4.316	1.8268	2.2
	Ni-O	5.311	1.9973	1.9
MnFeCoNiCu LDH	Ni-O	5.997	1.9809	2.0

N, coordination number; R, bonding distance; σ^2, Debye-Waller factor.

Error bars that characterize the structural parameters obtained by EXAFS spectroscopy were estimated as N ± 21%; R ± 1%; σ^2 ± 21%.

Table S3. Stability comparison of Au_{SA}-MnFeCoNiCuOOH and other LDHs/oxyhydroxides OER catalysts.

Sample	Current density (mA cm^{-2})	Time (h)	Decay	Ref.
Au_{SA}-MnFeCoNiCu LDH	**100**	**700**	**6.4%**	**This work**
FeOOH/NiFe-LDH	100	700	14.1%	[1]
CoCuFeMoOOH	10/20/50	72	almost no decay	[2]
EA-FCCN	400	20	7%	[3]
HEH	10	25	negligible loss	[4]
HF-HEA-a	10	11	-	[5]
AN-CuNiFe	10	12	-	[6]
HEAN@NPC/CC-450	10	24	-	[7]
CrZnFeCoNi HEHs	70	12	no obvious decay	[8]
Fe-Cr-Co-Ni-Cu HE-LDHsAr-20	10	16	-	[9]
NiFe-LDH/Ti_3C_2Tx/NF	50	15	-	[10]

NiFe LDH	30	24	without any noticeable loss	[11]
NiFe LDH/V–Co_4N@NF	10/20/50/100	25	-	[12]
NiO@NiFeLDH/NF-US	50/100	50	-	[13]
NH_3-Fe^{2+} Ni^{2+} -Fe25Ni75	100	24	-	[14]
Ni_3FeW LDH/NF	100	50	-	[15]

Table S4. Calculated LHB values of MnFeCoNiCuOOH and Au_{SA}-MnFeCoNiCuOOH.

	Mn	Fe	Co	Ni	Cu
MnFeCoNiCuOOH	-2.732	-2.604	-2.634	-2.615	-2.463
Au_{SA}-MnFeCoNiCuOOH	-2.791	-2.801	-2.766	-2.813	-2.783

Table S5. Calculated ΔU values of MnFeCoNiCuOOH and Au_{SA}-MnFeCoNiCuOOH.

	Mn	Fe	Co	Ni	Cu
MnFeCoNiCuOOH	3.666	3.524	3.864	3.895	3.662
Au_{SA}-MnFeCoNiCuOOH	3.918	3.923	4.019	4.032	4.009

Table S6. Calculated Gibbs free energy (ΔG) values (U=1.23 V) in AEM on the Mn, Fe, Co, Ni, Cu sites of MnFeCoNiCuOOH and Au_{SA}-MnFeCoNiCuOOH.

	site	ΔG_{*OH} (eV)	ΔG_{*O} (eV)	ΔG_{*OOH} (eV)
MnFeCoNiCuOOH	Mn	-0.91	-1.21	0.65
	Fe	-0.89	-1.38	0.39

	Co	-0.59	-1.51	0.42
	Ni	-0.15	-1.36	0.44
	Cu	-1.03	-1.15	0.67
Au_{SA}-MnFeCoNiCuOOH	Mn	-0.03	-1.28	0.50
	Fe	-0.81	1.11	0.4
	Co	-0.52	-1.32	0.42
	Ni	-0.70	-1.38	0.11
	Cu	-0.65	-1.22	0.37

Table S7. Calculated Gibbs free energy (ΔG) values in LOM of MnFeCoNiCuOOH with only O vacancy, MnFeCoNiCuOOH with only Au atom, MnFeCoNiCuOOH and Au_{SA}-MnFeCoNiCuOOH.

	ΔG_{*O} (eV)	ΔG_{*OOH} (eV)	ΔG_{*OO} (eV)	ΔG_{Vo} (eV)
MnFeCoNiCuOOH with only O vacancy	1.23	2.05	0.73	-0.11
MnFeCoNiCuOOH with only Au atom	1.17	2.19	0.23	-0.92
MnFeCoNiCuOOH	1.77	2.25	1.56	-1.13
Au_{SA}-MnFeCoNiCuOOH	1.14	2.08	1.66	0.38

References

1. Liang, Y.*, et al.* Ultrafast Fenton-like reaction route to FeOOH/NiFe-LDH heterojunction electrode for efficient oxygen evolution reaction. *J. Mater. Chem. A* **9,** 21785-21791 (2021).
2. Zhang, L., Cai, W., Bao, N. Top-Level Design Strategy to Construct an Advanced High-Entropy Co–Cu–Fe–Mo (Oxy)Hydroxide Electrocatalyst for the Oxygen Evolution Reaction. *Adv. Mater.* **33,** 2100745 (2021).
3. Zhang, N.*, et al.* Lattice oxygen activation enabled by high-valence metal sites

for enhanced water oxidation. *Nat. Commun.* **11,** 4066 (2020).

4. Zhang, T.*, et al.* Boosting the oxygen evolution electrocatalysis of high-entropy hydroxides by high-valence nickel species regulation. *ChemComm* **58,** 7682-7685 (2022).

5. Ma, P.*, et al.* Hydroxylated high-entropy alloy as highly efficient catalyst for electrochemical oxygen evolution reaction. *Sci. China Mater.* **63,** 2613-2619 (2020).

6. Cai, Z.*, et al.* Amorphous Nanocages of Cu-Ni-Fe Hydr(oxy)oxide Prepared by Photocorrosion For Highly Efficient Oxygen Evolution. *Angew. Chem. Int. Ed.* **58,** 4189-4194 (2019).

7. Huang, K.*, et al.* Exploring the impact of atomic lattice deformation on oxygen evolution reactions based on a sub-5 nm pure face-centred cubic high-entropy alloy electrocatalyst. *J. Mater. Chem. A* **8,** 11938-11947 (2020).

8. Yu, X.*, et al.* 2D High-Entropy Hydrotalcites. *Small* **17,** 2103412 (2021).

9. Gu, K.*, et al.* Ultrathin defective high-entropy layered double hydroxides for electrochemical water oxidation. *J. Energy Chem.* **60,** 121-126 (2021).

10. Si, H.*, et al.* Hydrophilic NiFe-LDH/Ti_3C_2Tx/NF electrode for assisting efficiently oxygen evolution reaction. *J. Solid State Chem.* **295,** 121943 (2021).

11. Suliman, M.*, et al.* Growth of ultrathin nanosheets of nickel iron layered double hydroxide for the oxygen evolution reaction. *Int. J. Hydrog. Energy* **47,** 23498-23507 (2022).

12. Zhang, S.*, et al.* Heterointerface enhanced NiFe LDH/V–Co_4N electrocatalysts

for the oxygen evolution reaction. *J. Mater. Chem. A* **10,** 21523-21530 (2022).

13. Sirisomboonchai, S.*, et al.* Fabrication of NiO Microflake@NiFe-LDH Nanosheet Heterostructure Electrocatalysts for Oxygen Evolution Reaction. *ACS Sustain. Chem. Eng.* **7,** 2327-2334 (2019).

14. Chen, Z.*, et al.* Revealing the Formation Mechanism and Optimizing the Synthesis Conditions of Layered Double Hydroxides for the Oxygen Evolution Reaction. *Angew. Chem. Int. Ed.* **62,** e202215728 (2023).

15. Wu, L.*, et al.* Facile synthesis of nanoparticle-stacked tungsten-doped nickel iron layered double hydroxide nanosheets for boosting oxygen evolution reaction. *J. Mater. Chem. A* **8,** 8096-8103 (2020).